Differential interfacial tension between oncogenic and wild-type populations forms the mechanical basis of tissue-specific oncogenesis in epithelia

Amrapali Datta[1], Phanindra Dewan[2], Aswin Anto[1], Tanya Chhabra[3], Tanishq Tejaswi[1], Sindhu Muthukrishnan[1], Akshar Rao[1], Sumantra Sarkar[2], Medhavi Vishwakarma[1]*

[1]Department of Bioengineering, Indian Institute of Science, Bengaluru, India

[2]Department of Physics, Indian Institute of Science, Bengaluru, India

[3]Department of Physics, Syracuse University, Syracuse, USA

Correspondence: medhavi@iisc.ac.in

Keywords: tissue-specific oncogenesis, interfacial tension, mechanical interactions, epithelial tissue mechanics, oncogenic clusters, cell competition.

Abstract

Why does the same oncogenic mutation drive tumor formation in some tissues but not in others? While cancer driver mutations are well-documented, their tissue-specific effects remain largely attributed to genetic factors, leaving the biophysical aspects underexplored. Here, we demonstrate that mechanical interactions, specifically interfacial tension between newly transformed and wild-type epithelial cells are critical in determining survival and growth of $HRas^{V12}$ oncogenic mutants in human mammary and bronchial epithelia, leading to contrasting outcomes in the two tissues. In mammary epithelium, isolated oncogenic cells are extruded- a typical mechanism of defense against cancer in epithelia- while oncogenic groups become spatially confined in a kinetically arrested, jammed state, marked by an actomyosin belt at the interface. In contrast, bronchial epithelium permits persistent spreading of the same oncogenic cells, which form long protrusions regardless of colony size. Furthermore, oncogenic clusters in these two tissues exhibit distinct biophysical properties, including variations in cell shapes, intracellular pressure, cell-cell tension, and cellular motility. Using a cell shape-tension coupled bi-disperse vertex model, we reveal that differences in interfacial tension at mutant–wild-type boundaries dictate whether oncogenic cells are eliminated, restrained, or expanded and that modulating interfacial tension alters mutant cell fate within the epithelium. Together, our findings uncover a mechanical basis for tissue-specific oncogenesis by highlighting how differential cellular mechanics at the oncogenic–host cell interface regulate tumor initiation and progression.

Introduction

Cancer has traditionally been understood to be a consequence of deregulated cell proliferation driven by genetic alterations that enable clonal expansion and tumor formation [1]. Interestingly, genomic analysis reveals that many tumor suppressor genes and oncogenes exhibit tissue specificity, meaning they are altered in some cancers but not others [2-4]. Current research suggests that a combination of intrinsic biological factors [4], such as differential epigenetic changes [3,5] and aneuploidy patterns [6-8], as well as extrinsic factors like the tumour microenvironment, including the presence of tissue-specific immune cells [9-10] influences tissue-specific cancer outcomes. However, a relatively underexplored yet crucial aspect of tissue-specific oncogenesis is the mechanical interaction between normal and cancerous cells. To this end, recent studies have highlighted a tumor suppressive behavior in epithelial tissues known as epithelial defense against cancer (EDAC) [11], where transformed cells are expelled from the tissue by surrounding normal cells [12-14]. However, EDAC can fail [14], allowing mutant cells to evade extrusion when the microenvironment becomes tumour-permissive, such as in conditions of increased stiffness [15] or inflammation due to a high-fat diet [16]. The success or failure of EDAC is closely linked to changes in cellular contractility [12-14] and cell-cell adhesions [17], suggesting that the underlying biophysical properties of the tissue play a decisive role in determining the outcome of cell competition. Since these properties can vary across different epithelial tissues, tissue-specific differences in cancer susceptibility may be explained by the varying ability of epithelia to manage newly transformed cells. However, despite these advances, the mechanical basis of tissue-specific oncogenesis remains missing. Specifically, how differences in cellular mechanics at the interface between oncogenic and wild-type populations influence tumor initiation and progression is poorly understood. Addressing this gap could not only enhance our understanding of cancer biology but also open new avenues for tissue-specific therapeutic interventions by identifying what makes certain tissues more permissive to tumor formation.

To this end, we investigated and compared the bio-physical factors influencing early tumorigenesis in human mammary and bronchial epithelial monolayers by sporadically transfecting a subset of healthy cells into oncogenic cells expressing a constitutively active $HRas^{V12}$ protein. We then tracked the fate of these transfected cells and their interactions with the wild-type counterparts in real time via live imaging. Strikingly, $HRas^{V12}$-mutant cells exhibited contrasting behaviors in the

two tissues. In breast epithelium, isolated transformed cells were frequently extruded. However, when present in groups, extrusion of oncogenic cells was not seen, but instead, they remained spatially confined in a jammed state. In contrast, in lung epithelium, single as well as groups of $HRas^{V12}$ expressing cells persisted and exhibited unrestricted expansion over time, regardless of cluster size. To explain these findings, we employed a bi-disperse vertex model of epithelia [18-21] and demonstrated that differences in interfacial tension between wild-type and transformed populations play a crucial role in determining whether mutant cells are eliminated, restrained, or are allowed to persist and expand. Taken together, these findings provide novel insights into the differential outcomes of competitive cellular interactions in the precancer stages and uncover a mechanical basis for tissue-specific oncogenesis.

Results:

1. Singlets and groups of $HRas^{V12}$ oncogenic mutants show tissue-specific fates in epithelia.

To explore the differences in the premalignant stages across epithelial tissues, we sporadically transfected monolayers of the two non-transformed human epithelial cell lines, Mcf10a (mammary) and Beas2b (bronchial), with a plasmid construct that constitutively expresses $HRas^{V12}$ along with the GFP reporter. We then monitored the cellular dynamics over 90 hours. Consistent with previous studies reporting extrusion of single $HRas^{V12}$ mutants in MDCK monolayers [11-15, 22], we observed that isolated $HRas^{V12}$ transfected cells (singlets) surrounded by wild-type neighbours were extruded from the mammary epithelium [Figure. 1b, Supplementary video 1]. This process correlated with a reduction in shape indices of oncogenic mutants as the density of wild-type cells around them increased [Figure. 1d (upper panel)]. Interestingly, this well-known mechanism of epithelial defense against cancer was impaired in Beas2b cells, where $HRas^{V12}$ mutants evaded extrusion [Figure. 1c, e], and wild-type cell compaction did not restrict their growth [Figure. 1c]. Instead, the mutants in the bronchial epithelium continued to proliferate and exhibited increased elongation with long protrusions [Figure. 1c (lower panel), Supplementary video 2]. Given that cancers frequently arise from fields of oncogenic mutants rather than isolated mutated cells [23-25], we also investigated whether these differential dynamics of mutant singlets would also extend to groups of oncogenic mutants, potentially enabling more aggressive $HRas^{V12}$ growth in lung tissue compared to breast tissue. By adjusting cell seeding conditions, we generated larger groups of $HRas^{V12}$ transfected cells in both Mcf10a and Beas2b monolayers and then tracked

91 the dynamics of these groups over time. In the mammary epithelium, wild-type cells were unable
92 to extrude groups of HRas^{V12}-transfected cells but instead confined them into compact, circular
93 clusters with smooth, rounded interfaces [Figure 1g, (upper panel), i (upper panel)] Supplementary
94 Video 3]. As a result, oncogenic clusters gradually demixed from the surrounding wild-type
95 Mcf10a population and remained spatially constrained [Figure 1j]. In contrast, HRas^{V12} clusters in
96 the bronchial epithelium gradually spread outward [Figure. 1h, j, Supplementary video 4], form
97 protrusive lamellipodia, grow on top of one another [Figure. 2b] and develop an irregular interface
98 with surrounding wild-type cells [Figure 1h, i (lower panel)]. Together, these striking differences
99 in the dynamics of HRas^{V12} oncogenic cells demonstrate that activation of the same oncogene can
100 lead to distinct outcomes across tissues in terms of growth, spreading, and extrusion. This
101 prompted us to further investigate the unique bio-physical mechanisms driving these variations.
102

103 *2. Biophysical analysis reveals demixing via jamming of oncogenic clusters in Mcf10A but*
104 *unjamming and protrusive growth in Beas2b.*

105 To understand the mechanisms driving the differential fates of oncogenic fields in the two
106 epithelial tissues, we mapped the bio-physical signatures of wild-type-mutant interactions by
107 subdividing the images into four regions of interests for both monolayers- ROI1: wild type cells
108 distant from oncogenic cells, ROI2: interfacial wild type cells in direct contact with oncogenic
109 cells, ROI3: oncogenic cells at the cluster boundaries in direct contact with wild type cells, and
110 ROI4: oncogenic cells in contact with other oncogenic cells [Figure. 2a]. We then compared the
111 F-actin levels and shapes of both mutant and wild-type populations across these ROIs.
112 Additionally, we employed Bayesian force inference, as previously established [26], to infer the
113 differential tissue stresses associated with cluster formation from the observed cell geometries.
114 Interestingly, the differences across these parameters were apparent not only between wild-type
115 and oncogenic counterparts but also based on the spatial localization of the cells, with cells at the
116 oncogenic-wild type interface exhibiting distinct behaviors, regardless of their origin.
117 In mammary epithelium, oncogenic clusters were surrounded by a prominent actin belt [Figure.
118 2b (upper panel), c (upper panel)], coupled with drastically low F-actin levels inside the clusters
119 [Figure. 2e (left panel)], suggesting that the de-mixing of oncogenic cells in breast tissue is likely
120 driven by changes in cellular mechanics. Further, oncogenic clusters in mammary epithelium

(ROI4) also exhibited low cell shape indices [Figure. 2d (upper panel), f (left panel)], high internal pressure [Figure. 2h (upper panel), j (upper panel)], and low line tension [Figure. 2h (upper panel), j (lower panel)]- characteristics indicative of jamming [27]. Notably, both oncogenic cells and wild-type Mcf10a cells at the cluster interface (ROI 2 and ROI3) showed F-actin enrichment, while the interfacial wild shape cells show elongated shapes [Figure. 2e (left panel), f (left panel)], indicating that interfacial cellular mechanics play a key role in the de-mixing process as the wild-type cells encircle the oncogenic mutants. This interfacial region enriched with F-actin also contained phosphomyosin [Supplementary Figure. 1a], indicating that a contractile actomyosin belt drives the compaction of oncogenic clusters in mammary epithelia. In contrast, bronchial epithelium exhibited no actin belt formation at the wild type-oncogenic cell interface, and no traits of jamming were observed in the oncogenic clusters [Figure. 2b (lower panel), c (lower panel)]. Instead, oncogenic cells continued to proliferate, displaying elongation measured via higher shape indices and high F-actin expression [Figure. 2d (lower panel), e (right panel), f (right panel)]- indicative of unjamming behaviour [27,28]. The relative internal cell pressure and cell-cell line tension inferred with Bayesian force inference showed slight or no modulation in the oncogenic clusters, given the general elongated shapes of wild-type cells in Beas2b cells [Figure. 2i, j]. Together, these findings highlight distinct interfacial mechanics between oncogenic cells and their wild-type neighbors in both Mcf10A and Beas2b monolayers, resulting in differing outcomes in mutant colony growth.

3. PIV analysis reveals kinetic arrest of oncogenic clusters in mcf10a coupled with tangential motion of interfacial cells

To further probe the cellular dynamics that lead to the contrasting fates of the oncogenic mutant colonies in the two tissues, we analyzed cellular velocities during the de-mixing of oncogenic cells, using Particle Image Velocimetry (PIV) on consecutive image pairs from mammary and bronchial monolayers. Interestingly, velocity maps in samples imaged for mutant – wild type dynamics in Mcf10a [Supplementary video 5] revealed an unusual movement pattern at confluency: wild type Mcf10a cells exhibited tangential motion around oncogenic clusters [Figure. 3b], which coupled with a drastic reduction in the velocity of oncogenic cells [Figure. 3a], likely caused their compaction and jamming into clusters. Notably, this tangential movement was unique to wild-type Mcf10a cells surrounding oncogenic clusters and was absent in other regions across the monolayer

[Figure. 3b] as well as under control conditions- i.e., in the absence of oncogenic mutants [Supplementary video 6], in both of which a typical velocity drop was observed in Mcf10a cells due to density-induced jamming [27-30] [Figure. 3d (upper panel), Supplementary 2, Supplementary video 6]. These results aligned with the observed differences in cell shape indices, where oncogenic clusters underwent jamming, while wild-type cells at the interface exhibited unjamming behavior [29,30]. In contrast, in the bronchial epithelium, mutant clusters remained unjammed, even as surrounding wild-type cells became more crowded [Figure. 3c, d (lower panel), Supplementary video 7]. Additionally, no tangential cellular movement was detected around the oncogenic clusters in the bronchial epithelium. These velocity maps showed negligible deviations from wild-type (control) beas2b velocity maps [Supplementary video 8]. Together, these findings suggest that mutant clusters carrying the same oncogene can exhibit drastically different behaviors depending on the epithelial tissue type. Specifically, differences in the dynamics of the interfacial cells drive the demixing and jamming of HRasV12 oncogenic cells in mammary epithelium while promoting protrusive, unjammed growth in bronchial epithelium.

4. Bi-disperse vertex model reveals differential interfacial tension between mutant and wild-type population governs tissue-specific response towards oncogenic mutants

To explain the differential dynamics and degrees of demixing of oncogenic clusters observed in the two tissues, we drew inspiration from the differential interfacial tension hypothesis (DITH) [31]. This hypothesis suggests that cell sorting in tissues could occur due to the variations in interfacial tension, as seen in embryonic cell rearrangement, where cells regulate contractility, as well as adhesions to demix from their neighbors [31-33]. To test whether such a mechanism could be applied to the de-mixing of oncogenic clusters from wild-type cells- leading to tissue-specific outcomes, we employed the cell-based bi-disperse Vertex Model (VM). Our model allowed us to simulate an epithelial monolayer and capture the dynamic interactions between wild-type and mutant cell populations. We analyzed the mechanics underlying the segregation dynamics of mutant clusters by examining the interfacial line tension $\Lambda_{ij}^{M/WT}$ between the oncogenic and wild-type cells [Fig. 4a]. In our model, $\Lambda_{ij} = 0$, for homotypic interfaces, i.e. wild-type-wild type or mutant-mutant interactions, and $\Lambda_{ij} = \Lambda \neq 0$, for heterotypic interfaces between oncogenic and wild type cells. When $\Lambda > 0$, our model ensures that the interface between oncogenic and healthy cells contracts to minimize energy, leading to a reduction in total interfacial length, and when $\Lambda < 0$, our model

promotes a rough interface by favouring increased interface between healthy and oncogenic cells [Supplementary Video 9]. The final interface shape is determined by the balance between interfacial tension and the intrinsic perimeter and area elasticity of individual cells [Fig. 4b].

To explain the observed differences in interfacial cellular dynamics, we introduced an active contribution to interfacial tension, which was coupled to the shape of cells at the interface, called shape-tension coupling [34]. This active interfacial tension is extensile, meaning it elongates cells along the interface depending on their orientation relative to the interface. It originates from the anisotropic distributions of stress fibres when cells are under external stress. Hence, we assume that it becomes significant only when the hydrostatic pressure on the interfacial cells exceeds a threshold value Π_0 [Fig. 4b, g].

Remarkably, our model robustly captured the experimentally observed behaviors. As a first check, we compared the experimentally observed differences in the shape indices between interfacial and non-interfacial wild-type and oncogenic cells in both mammary and lung epithelium with our model's predictions. For $\Gamma = 0.2, \Pi_0 = \{0, 0.1, 0.3\}$, $\Lambda = \{0 - 1.6\}$, our model accurately captured the experimental observations [Fig. 4c]. For stress threshold values lower than $\Pi_0 = 0.3$, we find that the differences in shape indices are non-zero even for $\Lambda = 0$, which is an unphysical situation. This is unphysical because we expect there to be no difference in the shape indices because in principle, there is only one cell type for $\Lambda = 0$. Thus, we have taken $\Pi_0 = 0.3$ for further analyses. To make the comparison between the model and the experiment more robust, we compared other metrics as well.

To quantify the extent of mixing between wild-type and mutant cells, we used the demixing parameter (DP), defined as: $\mathrm{DP} = \langle DP_j \rangle = \left\langle 2\left(\frac{N_s}{N_t} - \frac{1}{2}\right)\right\rangle$, where N_s represents the number of same-type neighbours, and N_t is the total number of neighbours of a given cell[35]. Our simulations showed that when $\Lambda < 0$ the demixing parameter rapidly decreases over time, indicating outward protrusion of the mutant cluster. In contrast, for $\Lambda > 0$ the demixing parameter remained close to 1, reflecting a compact, jammed cluster [Fig. 4f]. Additionally, we observed that when $\Lambda > 0$, cells within the cluster experience higher internal pressure compared to when $\Lambda < 0$ [Fig 4g], consistent with experimental findings [Fig. 2h, i]. Furthermore, flow field analysis from our

simulations [Fig 4h, i] revealed that for $\Lambda > 0$, cell movement aligns tangentially along the cluster boundary—consistent with the Mcf10A behaviour—whereas for $\Lambda < 0$ cell motion was uniform throughout the monolayer, resembling the Beas2b phenotype [Fig 3b]**.** These comparions further establish that different values of Λ correspond to different cell types. The same oncogene thus might affect different cell lines differently. We also estimated the probability of single mutant cell extrusion as a function of Λ [Fig 4j], consistent with the findings from our experiments which show that isolated $HRas^{V12}$ transfected cells are frequently extruded in mammary tissue [Fig 1b]. Together, our findings demonstrate how interfacial tension-driven mechanics could play a crucial role in determining the competitive dynamics between wild-type and mutant populations, thus providing compelling evidence that cellular and tissue mechanics are key determinants of cell competition.

5. *Disrupting actomyosin belt using blebbistatin prevents demixing and compaction of mutant clusters in mammary epithelia*

Since our model showed that differences in interfacial tension regulate mutant cluster dynamics, with a higher interfacial tension driving cluster compaction [Supplementary video 9], we reasoned that this tension is mediated by the supracellular actomyosin belt [36] that drives the compaction and segregation of oncogenic clusters in mammary epithelium. Therefore, we investigated whether disrupting the cytoskeletal organization and impairing actomyosin belt formation would affect the demixing and compaction of oncogenic clusters. To test this, we treated Mcf10a monolayers with 5 μM blebbistatin, a myosin II inhibitor, to disrupt belt formation.

As expected, blebbistatin treatment prevented mutant cluster compaction [Figure. 5a], leading to a loss of their rounded morphology and restoring actin levels and shape indices of mutant cells to wild-type levels [Figure. 5b]. This shift resulted in mutant clusters resembling those observed in bronchial epithelia, suggesting that cytoskeletal organization plays a key role in tissue-specific differences in mutant cluster dynamics. This was also consistent with the fact that interfacial tension between cells arises from the interplay between the cortical actomyosin network and cell-cell adhesion [36].

Additionally, we looked into the inherent differences in cytoskeletal mechanics of the host tissues and observed distinct differences in actin organization between the two tissues. Wild-type bronchial epithelial cells exhibited higher F-actin intensities [Figure. 5c (upper panel), e] and had

241 longer stress fibers [Figure. 5c (middle panel), d (left panel)] compared to wild-type mammary
242 epithelial cells. These cytoskeletal differences were also coupled with significant differences in
243 cell shapes between confluent Mcf10a and Beas2b monolayers with wild-type beas2b cells
244 exhibited significantly higher shape indices, indicating elongated, loosely packed morphologies
245 and a lower degree of jamming [Figure 5d (right panel). In contrast, mammary epithelial cells had
246 lower shape indices, reflecting a more compact and tightly packed arrangement [Figure. 5d (right
247 panel)]. These differences were also in agreement with the PIV maps of the two wild-type tissues
248 [Supplementary figure 2, Supplementary videos 6 and 8] where the mammary monolayers
249 underwent a sharper drop in velocities and therefore kinetic arrest, compared to the bronchial
250 epithelia. Another key difference was in the strength of cell-cell adhesions. Bronchial epithelial
251 cells exhibited weaker cell-cell adhesions, as indicated by reduced E-cadherin staining intensity at
252 cell junctions compared to mammary epithelial cells [Figure. 5c (bottom panel), e]. These weaker
253 adhesions likely contributed to increased cellular motility and a diminished ability to constrain
254 mutant clusters, in contrast to the more stable, compacted clusters observed in mammary
255 epithelium. Together, these findings demonstrate that variations in mechanical properties-
256 including cell shape, actin organization, and adhesion strength- govern the differential responses
257 of mammary and bronchial epithelia to oncogenic mutants and may in turn, influence tumor growth
258 and progression.

259 **Discussion**

260 Our findings reveal a striking tissue-specific response to $HRas^{V12}$ oncogene activation in epithelial
261 monolayers, highlighting key differences in the growth, segregation, and mechanical behavior of
262 mutant clusters in mammary and bronchial epithelia. These insights shed light on the differential
263 susceptibility of epithelial tissues to oncogenic transformation and uncover a mechanical basis for
264 tissue-specific oncogenesis. By demonstrating how interfacial tension at the mutant-wild-type
265 boundary governs whether oncogenic cells are restrained or overgrow, our work shifts the focus
266 from purely molecular pathways to the biophysical constraints that regulate tumor initiation.

267 While previous studies have emphasized the contextual nature of tumorigenesis [2-4] and
268 highlighted the critical role of interactions between healthy and oncogenic cells during epithelial
269 cancer initiation [14, 22, 38], our work integrates and extends these perspectives by demonstrating

how interfacial tension at the mutant-wild-type boundary determines whether transformed cells remain constrained or undergo unchecked expansion.

$HRas^{V12}$ mutant clusters exhibited contrasting behaviors in mammary and bronchial epithelia. In the mammary epithelium, mutant clusters underwent demixing, and got restrained into compact, circular aggregates with smooth interfaces whereas in bronchial epithelia, they dispersed, exhibited protrusive growth, and formed jagged interfaces with surrounding wild-type cells. Bio-physical characterizations and PIV analysis revealed tissue specificity in cytoskeletal changes, and, subsequently cell shape changes, movement patterns, and internal pressures in both wild type and oncogenic populations, coupled with distinct mechanical behaviours of interfacial cells at the boundary of the two populations.

To probe the mechanistic basis of these differences, we applied the Differential Interfacial Tension Hypothesis (DITH) [31,32]and simulated mutant-wild-type interactions using a bi-disperse Vertex model. Our simulations demonstrated that interfacial tension is a key determinant of cluster morphology and compaction. When interfacial tension was positive, mutant clusters compacted into circular aggregates, recapitulating Mcf10A behavior. In contrast, negative interfacial tension ($\Lambda<0$) resulted in irregular, protrusive clusters that failed to compact, mirroring the Beas2b phenotype. Agreeing with our model, we showed that disrupting the interfacial actomyosin belt in the mammary epithelia disrupted the restraint on oncogenic clusters, preventing their demixing and compaction and shifting mutant behavior to a more unjammed state. These findings underscore the role of interfacial cellular mechanics in shaping oncogenic cell fate, with mammary epithelium imposing physical constraints that limit mutant expansion, while bronchial epithelium lacks such mechanical barriers, permitting unchecked growth.

By integrating mechanical constraints into models of cancer initiation, our study provides a framework for understanding how different epithelial tissues resist or permit tumorigenesis. However, while interfacial tension emerges as a key regulator of oncogenic segregation, the molecular pathways driving these mechanical differences remain to be elucidated. Future studies should investigate how targeting specific signaling networks or cytoskeletal components influence interfacial tension and whether modulating these factors could provide therapeutic benefits.

298 Additionally, extending this framework to other oncogenes and tissue types could further elucidate
299 the mechanical principles governing tumor initiation and progression.

300 **References:**

301 1. Hanahan D, Weinberg RA. 2000. The hallmarks of cancer. *Cell* 100:57–70.
302 doi:10.1016/S0092-8674(00)81683-9.
303 2. Schneider G, Schmidt-Supprian M, Rad R, Saur D. 2017. Tissue-specific tumorigenesis:
304 context matters. *Nat Rev Cancer* 17:239–253. doi:10.1038/nrc.2017.5.
305 3. Haigis KM, Cichowski K, Elledge SJ. 2019. Tissue-specificity in cancer: The rule, not the
306 exception. *Science* 363:1150–1151. doi:10.1126/science.aaw3472.
307 4. Bianchi JJ, et al. 2020. Not all cancers are created equal: Tissue specificity in cancer genes
308 and pathways. *Curr Opin Cell Biol* 63:135–143. doi:10.1016/j.ceb.2020.01.006.
309 5. Yamashita S, et al. 2018. Genetic and epigenetic alterations in normal tissues have
310 differential impacts on cancer risk among tissues. *Proc Natl Acad Sci U S A* 115:1328–
311 1333. doi:10.1073/pnas.1717960115.
312 6. Beroukhim R, et al. 2010. The landscape of somatic copy-number alteration across human
313 cancers. *Nature* 463:899–905. doi:10.1038/nature08822.
314 7. Zack TI, et al. 2013. Pan-cancer patterns of somatic copy number alteration. *Nat*
315 *Genet* 45:1134–1140. doi:10.1038/ng.2760.
316 8. Davoli T, et al. 2013. Cumulative haploinsufficiency and triplosensitivity drive aneuploidy
317 patterns and shape the cancer genome. *Cell* 155:948–962. doi:10.1016/j.cell.2013.10.011.
318 9. Salmon H, Remark R, Gnjatic S, Merad M. 2019. Host tissue determinants of tumour
319 immunity. *Nat Rev Cancer* 19:215–227. doi:10.1038/s41568-019-0125-9.
320 10. Lehmann B, et al. 2017. Tumor location determines tissue-specific recruitment of tumor-
321 associated macrophages and antibody-dependent immunotherapy response. *Sci*
322 *Immunol* 2:eaah6413. doi:10.1126/sciimmunol.aah6413.
323 11. Kajita M, Fujita Y. 2015. EDAC: Epithelial defence against cancer—cell competition
324 between normal and transformed epithelial cells in mammals. *J Biochem* 158:15–23.
325 doi:10.1093/jb/mvv049.
326 12. Ohoka A, et al. 2015. EPLIN is a crucial regulator for extrusion of RasV12-transformed
327 cells. *J Cell Sci* 128:781–789. doi:10.1242/jcs.159772.

13. Kajita M, et al. 2014. Filamin acts as a key regulator in epithelial defence against transformed cells. *Nat Commun* 5:4428. doi:10.1038/ncomms5428.
14. Hogan C, et al. 2009. Characterization of the interface between normal and transformed epithelial cells. *Nat Cell Biol* 11:460–467. doi:10.1038/ncb1853.
15. Pothapragada SP, et al. 2022. Matrix mechanics regulates epithelial defence against cancer by tuning dynamic localization of filamin. *Nat Commun* 13:218. doi:10.1038/s41467-021-27640-w.
16. Sasaki A, et al. 2018. Obesity suppresses cell-competition-mediated apical elimination of RasV12-transformed cells from epithelial tissues. *Cell Rep* 23:974–982. doi:10.1016/j.celrep.2018.03.108.
17. Leung CT, Brugge JS. 2012. Outgrowth of single oncogene-expressing cells from suppressive epithelial environments. *Nature* 482:410–413. doi:10.1038/nature10826.
18. Alt S, Ganguly P, Salbreux G. 2017. Vertex models: from cell mechanics to tissue morphogenesis. *Philos Trans R Soc Lond B Biol Sci* 372:20150520. doi:10.1098/rstb.2015.0520.
19. Barton DL, et al. 2017. Active vertex model for cell-resolution description of epithelial tissue mechanics. *PLoS Comput Biol* 13:e1005569. doi:10.1371/journal.pcbi.1005569.
20. Fletcher AG, et al. 2014. Vertex models of epithelial morphogenesis. *Biophys J* 106:2291–2304. doi:10.1016/j.bpj.2014.04.021.
21. Fletcher AG, Osborne JM, Maini PK, Gavaghan DJ. 2013. Implementing vertex dynamics models of cell populations in biology within a consistent computational framework. *Prog Biophys Mol Biol* 113:299–326. doi:10.1016/j.pbiomolbio.2013.09.003.
22. Gupta P, Kayal S, Tanimura N, Pothapragada SP, Senapati HK, Devendran P, Das T. 2024. Mechanical imbalance between normal and transformed cells drives epithelial homeostasis through cell competition. *bioRxiv*. doi:10.1101/2023.09.
23. Sinjab A, Han G, Wang L, Kadara H. 2020. Field carcinogenesis in cancer evolution: what the cell is going on? *Cancer Res* 80:4888–4891. doi:10.1158/0008-5472.CAN-20-2312.
24. Franklin WA, Gazdar AF, Haney J, Wistuba II, La Rosa FG, Kennedy T, Miller YE. 1997. Widely dispersed p53 mutation in respiratory epithelium. A novel mechanism for field carcinogenesis. *J Clin Invest* 100:2133–2137. doi:10.1172/JCI119748.

25. Curtius K, Wright NA, Graham TA. 2018. An evolutionary perspective on field cancerization. *Nat Rev Cancer* 18:19–32. doi:10.1038/nrc.2017.102.
26. Ishihara S, Sugimura K. 2012. Bayesian inference of force dynamics during morphogenesis. *J Theor Biol* 313:201–211. doi:10.1016/j.jtbi.2012.08.026.
27. Atia L, Bi D, Sharma Y, Mitchel JA, Gweon B, Koehler SA, Fredberg JJ. 2018. Geometric constraints during epithelial jamming. *Nat Phys* 14:613–620. doi:10.1038/s41567-018-0109-9.
28. Park JA, Kim JH, Bi D, Mitchel JA, Qazvini NT, Tantisira K, Fredberg JJ. 2015. Unjamming and cell shape in the asthmatic airway epithelium. *Nat Mater* 14:1040–1048. doi:10.1038/nmat4357.
29. Sadati M, Qazvini NT, Krishnan R, Park CY, Fredberg JJ. 2013. Collective migration and cell jamming. *Differentiation* 86:121–125. doi:10.1016/j.diff.2013.02.003.
30. Mitchel JA, Das A, O'Sullivan MJ, Stancil IT, DeCamp SJ, Koehler S, Park JA. 2020. In primary airway epithelial cells, the unjamming transition is distinct from the epithelial-to-mesenchymal transition. *Nat Commun* 11:5053. doi:10.1038/s41467-020-18841-7.
31. Foty RA, Steinberg MS. 2005. The differential adhesion hypothesis: a direct evaluation. *Dev Biol* 278:255–263. doi:10.1016/j.ydbio.2004.11.012.
32. Brodland GW. 2002. The differential interfacial tension hypothesis (DITH): a comprehensive theory for the self-rearrangement of embryonic cells and tissues. *J Biomech Eng* 124:188–197. doi:10.1115/1.1449491.
33. Canty L, Zarour E, Kashkooli L, François P, Fagotto F. 2017. Sorting at embryonic boundaries requires high heterotypic interfacial tension. *Nat Commun* 8:157. doi:10.1038/s41467-017-00146-x.
34. Rozman, J., Yeomans, J. M., & Sknepnek, R. (2023). Shape-tension coupling produces nematic order in an epithelium vertex model. *Physical Review Letters*, *131*(22), 228301.
35. Sahu, P., Sussman, D. M., Rübsam, M., Mertz, A. F., Horsley, V., Dufresne, E. R., ... & Schwarz, J. M. (2020). Small-scale demixing in confluent biological tissues. *Soft Matter*, *16*(13), 3325-3337.
36. Martin, A. C. (2010). Pulsation and stabilization: contractile forces that underlie morphogenesis. *Developmental biology*, *341*(1), 114-125.

388 37. Manning ML, Foty RA, Steinberg MS, Schoetz EM. 2010. Coaction of intercellular
389 adhesion and cortical tension specifies tissue surface tension. *Proc Natl Acad Sci U S*
390 *A* 107:12517–12522. doi:10.1073/pnas.1003743107.
391 38. Moruzzi M, Nestor-Bergmann A, Brennan K, Woolner S. 2019. Dysregulated wild-type
392 cell division at the interface between host and oncogenic epithelium. *bioRxiv*.
393 doi:10.1101/578146.
394 39. Schindelin J, Arganda-Carreras I, Frise E, Kaynig V, Longair M, Pietzsch T, Cardona A.
395 2012. Fiji: an open-source platform for biological-image analysis. *Nat Methods* 9:676–
396 682. doi:10.1038/nmeth.2019.
397 40. Stringer C, Wang T, Michaelos M, Pachitariu M. 2021. Cellpose: a generalist algorithm
398 for cellular segmentation. *Nat Methods* 18:100–106. doi:10.1038/s41592-020-01018-x.
399 41. Aigouy B, Umetsu D, Eaton S. 2016. Segmentation and quantitative analysis of epithelial
400 tissues. *Drosophila: Methods and Protocols* 227–239. doi:10.1007/978-1-4939-6371-
401 3_13.
402 42. Skamrahl M, Schünemann J, Mukenhirn M, Pang H, Gottwald J, Jipp M, Janshoff A. 2023.
403 Cellular segregation in cocultures is driven by differential adhesion and contractility on
404 distinct timescales. *Proc Natl Acad Sci U S A* 120:e2213186120.
405 doi:10.1073/pnas.2213186120.
406 43. Thielicke W, Sonntag R. 2021. Particle Image Velocimetry for MATLAB: Accuracy and
407 enhanced algorithms in PIVlab. *J Open Res Softw* 9:12. doi:10.5334/jors.334.
408

409 **Materials and methods**

410 *Cell culture*

411 Non-transformed human mammary epithelial cell line MCF10A were maintained in complete
412 medium composed of phenol-free Dulbecco's modified Eagle's medium (DMEM–F12, Gibco)
413 supplemented with 5% charcoal-stripped horse serum (Gibco), 10 U ml^{-1} penicillin and 10 µg
414 ml^{-1} streptomycin (Pen-Strep, Invitrogen), epidermal growth factor (20 ng/ml; PeproTech),
415 hydrocortisone (0.5 mg/ml; Sigma-Aldrich), cholera toxin (100 ng/ml; Sigma-Aldrich), and
416 insulin (10 µg/ml; Sigma-Aldrich) at 37°C in a humidified incubator with 5% CO2.
417 Non-transformed human bronchial epithelium BEAS2B epithelial cells were cultured in
418 Dulbecco's modified Eagle's medium (DMEM, Gibco) supplemented with GlutaMax (Gibco) and

419 5% fetal bovine serum (FBS, Gibco) along with 10 U ml^{-1} penicillin and 10 μg ml^{-1} streptomycin
420 (Pen-Strep, Invitrogen). Cells were maintained at 37 °C and 5% CO_2 unless mentioned otherwise.
421
422 *Cell seeding*
423 10^5 Cells were seeded on fibronectin-coated (10 μg ml^{-1}) glass bottom dishes (35 mm Cellvis) and
424 transfected once they reached 80% confluency (for singlets) and 60% confluency to get transfected
425 groups.
426
427 *Transfection*
428 Cells were transiently transfected with the $Hras^{V12}$- GFP expressing plasmid DNA (Addgene
429 #18780) using Lipofectamine 3000 (Invitrogen), following the manufacturer's protocol. Post-
430 transfection, confluent monolayers were either fixed and immuno-stained or imaged directly.
431
432 *Blebbistatin addition*
433 Blebbistatin was diluted to 5 μM final solution and added 48h post-transfection. Samples were
434 washed after 24 hours and fixed right away.
435
436 *Immunofluorescence*
437 Cells were fixed with 4% paraformaldehyde (ThermoFisher) diluted in 1X Phosphate buffered
438 saline (PBS, Sigma-Aldrich) for 15 minutes at room temperature. After washing away the fixative
439 with 1X PBS, cells were permeabilized with 0.3% TritonX-100 (Sigma-Aldrich) in 1X PBS. Non-
440 specific antibody binding was blocked by incubating the samples in blocking solution (2% Bovine
441 Serum Albumin (BSA Sigma-Aldrich) and 2% FBS in PBS) at room temperature for 45 minutes.
442 Further, cells were incubated with primary antibody prepared in blocking/staining solution
443 overnight at 4°C. Post primary antibodies incubation, cells were washed thrice with 1X PBS for 5
444 minutes per wash and incubated with secondary antibodies conjugated to Alexa fluor 555, Alexa
445 fluor 594 conjugated phalloidin and 4′,6-diamidino-2-phenylindole (DAPI) to mark the cell
446 nucleus, prepared in blocking/staining solution, for 2 hours at room temperature. Finally, the
447 samples were washed four times with 1X PBS for 5 minutes per wash before proceeding to
448 microscopy.
449

450 *Microscopy*

451 Fluorescence images were acquired using 20X objective and 63x oil-immersion objective of a
452 Zeiss Axio Observer 7 Inverted Microscope with a scientific-grade sCMOS camera by Iberoptics.
453 For live imaging, samples were set up on a stage-top incubator and maintained at 37°C and 5%
454 CO2 throughout imaging.

455

456 *Image Analysis*

457 Image analysis for this study was performed using Fiji [39] except bayesian force inference and
458 particle image velocimetry (PIV) analysis, which was performed in MATLAB (MathWorks).
459 Cellpose [40] was used to segment cells to get cell count, shape indices and actin intensitites for
460 each cell while Tissue Analyzer [41] was used to segment cells for force inference.

461

462 *Quantification of cluster eccentricity and segregation index*

463 The term 'eccentricity' expresses a size reduction in the contact with neighboring cells. It was
464 quantified as the ratio of the length of the minor axis to the major axis of an ellipse, with a value
465 closer to 0 indicating a more circular shape. Eccentricity quantifications were performed on fixed
466 and live tissues using outlines that were manually drawn and measured using Fiji.
467 The segregation index SI, defined as the average ratio of homotypic and all cell neighbors as
468 done previously [42], quantifies the demixing degree. To quantify the SI, cells of each type were
469 manually counted, and finally, to generate the plots, the SI was averaged over all GFP-labelled
470 cells in one frame.

471

472 *Bayesian Force Inference*

473 Bayesian force inference was done as described previously [26] to determine the relative cellular
474 pressures and cell-cell edge or line tension.

475

476 *Particle Image Velocimetry (PIV)*

477 Particle Image Velocimetry (PIV) was done using the PIV Lab package on MATLAB [43]. Velocity
478 maps were obtained by a 3-pass interrogation window of 128 × 128 pixels that halved after each
479 pass. Tangential velocities were obtained by drawing concentric circles radially outward from the

center to a point twice the radius of the mutant cluster and integrated over the entire circle using a custom python code. The output is the tangential velocity as a function of the circle.

Statistical analysis

Statistical analyses were carried out in GraphPad Prism 10. Statistical significance was calculated by Unpaired t-test with Welch's correction. p-values greater than 0.05 were considered to be statistically not significant. Scatter-bar plots were displayed as mean ± s.e.m. No statistical methods were used to set the sample size. Quantification was done using data from at least three independent biological replicates. For analysis involving live-imaging experiments, data were collected from three independent experiments. All the experiments with representative images were repeated at least three times.

Vertex Model

A bi-disperse model is used to demonstrate the role of interfacial tension between two types of cells, specifically the HRas^{V12} mutant and wild-type cells.

$$E_{VM} = \sum_{\alpha\in\mathrm{WT}}\left[\frac{K_\alpha^{\mathrm{WT}}}{2}\left(A_\alpha - A_\alpha^{0,\mathrm{WT}}\right)^2 + \frac{\Gamma_\alpha^{\mathrm{WT}}}{2}\left(P_\alpha - P_\alpha^{0,\mathrm{WT}}\right)^2\right] + \sum_{\alpha\in\mathrm{M}}\left[\frac{K_\alpha^{\mathrm{M}}}{2}\left(A_\alpha - A_\alpha^{0,\mathrm{M}}\right)^2 + \sum_\alpha \frac{\Gamma_\alpha^{\mathrm{M}}}{2}\left(P_\alpha - P_\alpha^{0,\mathrm{M}}\right)^2\right] + \sum_{<ij>}\Lambda_{ij}\, l_{ij}$$

The first two sums are included in the standard vertex model, whereas the last term is introduced in our model to account for interfacial interactions between cells. Specifically, $\Lambda_{ij} = 0$ for interfaces between the same cell types, and $\Lambda_{ij} = \Lambda$ between different cell types. Using a line tension term like Λl_{ij} in the vertex model energy, where the l_{ij} is the length of an interface edge, we can obtain both segregation and spreading dynamics just from energy minimization. This term has been described as heterotypic line tension (HLT)[42]. Due to energy minimization, heterotypic interface length is minimized for $\Lambda > 0$ and maximized for $\Lambda < 0$, leading to segregation of the two cell types in the former case and complete mixing of them in the latter case.

The mutant cluster in the experiments with Mcf10a cells showed an actin belt forming along the cluster interface, with the cells along the interface being more elongated than normal. This actin ring is important for the compaction of mutant clusters in the presence of wild-type cells in the

epithelial monolayer. An isotropic interfacial tension, such as the Λl_{ij} term in our model cannot capture such anisotropic behaviour. Recently, it has been proposed that such anisotropic behaviour can arise from the anisotropic distribution of the cytoskeletal filaments inside the cell[41]. The resulting active interfacial tension, called the shape-tension coupling, can generate elongated shapes as observed in the experiments. The elongated cells in the experiments indeed have anisotropic distributions of the stress fibres. Hence, we included the effect of shape-tension in our model. The total interfacial tension is $\Lambda_{ij} + \gamma_{ij}(t; \Pi_0)$, where Λ_{ij} is a time-independent, passive, isotropic tension and γ_{ij} is a time-dependent active tension that depends on the shape of the cells sharing the interface and requires a threshold stress Π_0 to be nonzero. The details of the shape-tension coupling is described in the interface. We find that a nonzero activation stress Π_0 is necessary to reproduce experimentally observed results.

Appendix

Vertex Model Simulation

To understand the cause and the dynamics of interaction between mutant and wild-type population in different epithelial monolayers during cancer initiation, we used a cell-based model of epithelial tissues called the vertex model. A monolayer in the vertex model has total energy given by:

$$\mathrm{E_{VM}} = \sum_{\alpha} \left[\frac{K_\alpha}{2}(A_\alpha - A_\alpha^0)^2 + \frac{\Gamma_\alpha}{2}(P_\alpha - P_\alpha^0)^2 \right]$$

In the above energy function, the constant parameters K_α is the area modulus which gives the area elasticity of each cell and Γ_α is the perimeter modulus which give the elasticity due to the actomyosin cortex. The gradient of this energy function gives the forces on each vertex of the cell, $\vec{F}^{(i)} = -\nabla_{\vec{r}^{(i)}} E_{VM}$, where $\vec{r}^{(i)}$ is the position of the *ith* vertex. The dynamics of each vertex position is given by the overdamped equation of motion:

$$\frac{d\vec{r}^{(i)}}{dt} = \vec{F}^{(i)} + \vec{F}_{act}^{(i)} + \vec{F}_{motility}^{(i)}$$

where $\vec{F}_{act}^{(i)}$ is any active force which might drive the system out of equilibrium. $\vec{F}_{motility}^{(i)}$ is a force which propels individual cells by $\vec{F}_{motility}^{(i)} = v_0 \vec{p}_\alpha$, where $\vec{p}_\alpha$is the polarity of a given cell given by $\vec{p}_\alpha = (\cos\theta_\alpha, \sin\theta_\alpha)$, where this angle θ_α performs rotational diffusion:

$$\partial_t \theta_\alpha = \sqrt{2D_r}\, \eta_\alpha(t)$$

where $\eta_\alpha(t)$ is a Gaussian white noise with zero mean and correlation $\langle \eta_\alpha(t)\eta_{\alpha'}(t')\rangle = \delta(t-t')\delta_{\alpha\alpha'}$.

To capture the dynamics of cell segregation between two different types of cells in a monolayer of normal and oncogenic cells, we can use a bi-disperse vertex model with an interfacial line tension between the two types of cells - called mutant and wild type can be used.

The director of each cell corresponds to the polarization direction of the cell, which can be obtained as the larger eigenvector of its shape tensor, $\underline{\underline{G_\alpha}} = \frac{1}{N^{(\alpha)}}\sum_{i\in v_\alpha}\left(\vec{r}^{(i)} - \vec{r}_0^{(\alpha)}\right) \otimes \left(\vec{r}^{(i)} - \vec{r}_0^{(\alpha)}\right)$, where the sum is over $N^{(\alpha)}$ vertices of the cell α, and $\vec{r}_0^{(\alpha)}$ is the position of the cell's geometric center. The energy function for the vertex model used is given below:

$$E_{VM} = \sum_{\alpha\in \mathrm{WT}}\left[\frac{K_\alpha^{\mathrm{WT}}}{2}\left(A_\alpha - A_\alpha^{0,\mathrm{WT}}\right)^2 + \frac{\Gamma_\alpha^{\mathrm{WT}}}{2}\left(P_\alpha - P_\alpha^{0,\mathrm{WT}}\right)^2\right] + \sum_{\alpha\in \mathrm{M}}\left[\frac{K_\alpha^{\mathrm{M}}}{2}\left(A_\alpha - A_\alpha^{0,\mathrm{M}}\right)^2 + \sum_\alpha \frac{\Gamma_\alpha^{\mathrm{M}}}{2}\left(P_\alpha - P_\alpha^{0,\mathrm{M}}\right)^2\right] + \sum_{<ij>}\Lambda_{ij}\, l_{ij}$$

Here, M denotes mutant cells and WT denotes wild-type cells. The index α denotes cells, and the indices i, j denote vertices and $< ij >$ denotes an edge between vertices i and j. The parameters K_α^M, K_α^{WT} are the area moduli, Γ_α^M, Γ_α^{WT} are the perimeter moduli of the mutant and wild type respectively, and the Λ_{ij} denotes the interfacial line tension. This interfacial line tension is only along junctions connecting two vertices and depends on the cell type on either side of the junction. Since the system we are considering is bi-disperse, the interfacial line tension can have three values, depending on the identities of cells on either side of a given edge $< ij >$:

$$\Lambda_{\mathrm{ij}} = \begin{cases} \Lambda_{ij}^{\mathrm{M/M}} \text{ if both are mutant cells} \\ \Lambda_{ij}^{\mathrm{WT/WT}} \text{ if both are wild-type cells} \\ \Lambda_{ij}^{\mathrm{WT/M}} \text{ if one is wild-type and the other is mutant} \end{cases}$$

Shape-tension coupling

In addition to this passive interfacial tension, we can also have an active contribution coming from the shape tension coupling. The shape-tension coupling is mathematically the same as the passive line tension force. The total force is given by:

$$\left(\Lambda + \gamma_{ij}(t)\right)\vec{\nabla} l_{ij}$$

$\gamma_{ij}(t)$ depends on the relative orientation of the cell's director $\vec{n}$ and the edge along which the tension acts, $\vec{l}_{ij}$.(fig) Specifically, it has a relaxational dynamics of the form:

$$\dot{\gamma_{ij}} = \left[\gamma_{ij}(t) - \gamma_{ij_0}\right] / \tau.$$

Here $\gamma_{ij_0} = -\frac{1}{2}\zeta[\cos 2\theta + \cos 2\theta']$ couples the tension along an edge to the shape of the cells on either side of the edge [Supplementary figure 3]. For $\zeta > 0$, this tension is extensile and leads to the elongation of cells along the boundary. This happens because for the edges which have $\vec{n}$ and $\vec{n}'$ aligned with the edge vector (θ or $\theta' = 0, \pi, 2\pi$), the shape-tension coupling contributes a negative line tension, which favours this alignment. When the edge vectors are not aligned with the edge vector, the contribution is positive, and that edge starts to shrink. Eventually, the interface consists of cells whose directors are always aligned with the interface. Energetically, it counteracts interfaces with $\Lambda > 0$, leading to the formation of elongated cells and tangential flows along the interface. Importantly, we find that cell elongation correlates with the formation of actin belt, leading us to postulate that the shape-tension coupling is activated above a threshold pressure, Π_0, where the cell pressure is given by $\Pi = -\frac{\partial E_{VM}}{\partial A}$, When $\Lambda < 0$, such as in the Beas2b cells, we do not observe strong stress-fibre expression. Hence, we believe that it is not activated in those cells.

Simulation Setup

The vertex model energy can be nondimensionalised by setting a length scale set by $\sqrt{A^0}$. In our simulation we have taken

$$A_\alpha^{0,WT} = A_\alpha^{0,M} = A^0 \quad \forall\, \alpha$$

and

$$P_\alpha^{0,WT} = P_\alpha^{0,M} = P^0 \quad \forall\, \alpha.$$

Also,

$$K_\alpha^{WT} = K_\alpha^{M} = K \;\forall\, \alpha,$$

$$\Gamma_\alpha^{WT} = \Gamma_\alpha^{M} = \Gamma \;\forall\, \alpha$$

and

$$\Lambda_{ij}^{M/M} = \Lambda_{ij}^{WT/WT} = 0 \;\forall < ij >, \Lambda_{ij}^{M/WT} = \Lambda \;\forall < ij >.$$

The non-dimensionalization has been done, which defines the normalized parameters $\overline{\Gamma} = \Gamma/KA^0$ $\overline{\Lambda} = \Lambda/K(A^0)^{3/2}$. (In further discussions, the normalized parameters will be represented by the symbols Γ and Λ.)

The monolayer modelled by the vertex model can be described by a single number, the shape index, defined by $q = P^0/\sqrt{A^0}$. Here too, in principle we could have different shape indices for the mutant and wild type cells, but we take them to be the same. Unless otherwise mentioned, we take $\Lambda^{M/M} = \Lambda^{WT/WT} = 0$ and $\Lambda^{WT/M} = \Lambda$.

To simulate the elongation of cells along the interface, $\zeta > 0$ is used for an active extensile contribution to the interfacial tension.

A box containing 20×20 cells has been used with mutant cells placed within a region (non-circular) from the center of the box. The vertices are arranged in a hexagonal lattice with random displacements added to the position of each vertex. Periodic boundary conditions were used to simulate a confluent monolayer.

Parameters:

K	1
Γ	0.1
A^0	1
P^0	4.0
l_{min} for T1 transitions	0.04
Δt for time stepping	0.01
v_0 for motility	0.05
D_r for rotational diffusion	0.5
ζ for shape-tension coupling	0.6

To prevent overlaps, a node switch operation is also added to the simulation, which changes the topology of the network[21].

Author contributions

M.V conceived the project. M.V. and A.D. designed experiments. A.D performed all experiments except the staining on Beas2b cells, which were performed by A.A. Theoretical model was contributed by P.D and S.S. Analysis and interpretation of experimental data was done by A.D, T.C, T.T, A.A, S.M, A.R and M.V. A.D and M.V developed and wrote the manuscript with help from P.D and S.S. All authors read, discussed and commented on the manuscript.

Acknowledgements

We thank Sriram R. Ramaswamy, and Tamal Das for critical discussions and suggestions. M.V is a partner group leader of the Max Planck Society (MPG), Germany, which has supported part of this work. This work is also supported by the Infosys foundation, Anusandhan National Research Foundation- previously called as Science and Engineering Research Board (project number: SERB SRG/2022/000534), and Indo German Science and Technology Centre (IGSTC WISER scheme). SS acknowledges funding from IISc, Axis Bank Center for Mathematics and Computing, and a startup grant from SERB-DST (SRG/2022/000163). We also acknowledge intramural funds at IISc Bangalore for providing support towards equipment and facilities and for salaries/fellowships of the authors.

Figure 1: ***Tissue-specific outcomes of HRas^{V12} oncogenic mutants in epithelial monolayers***

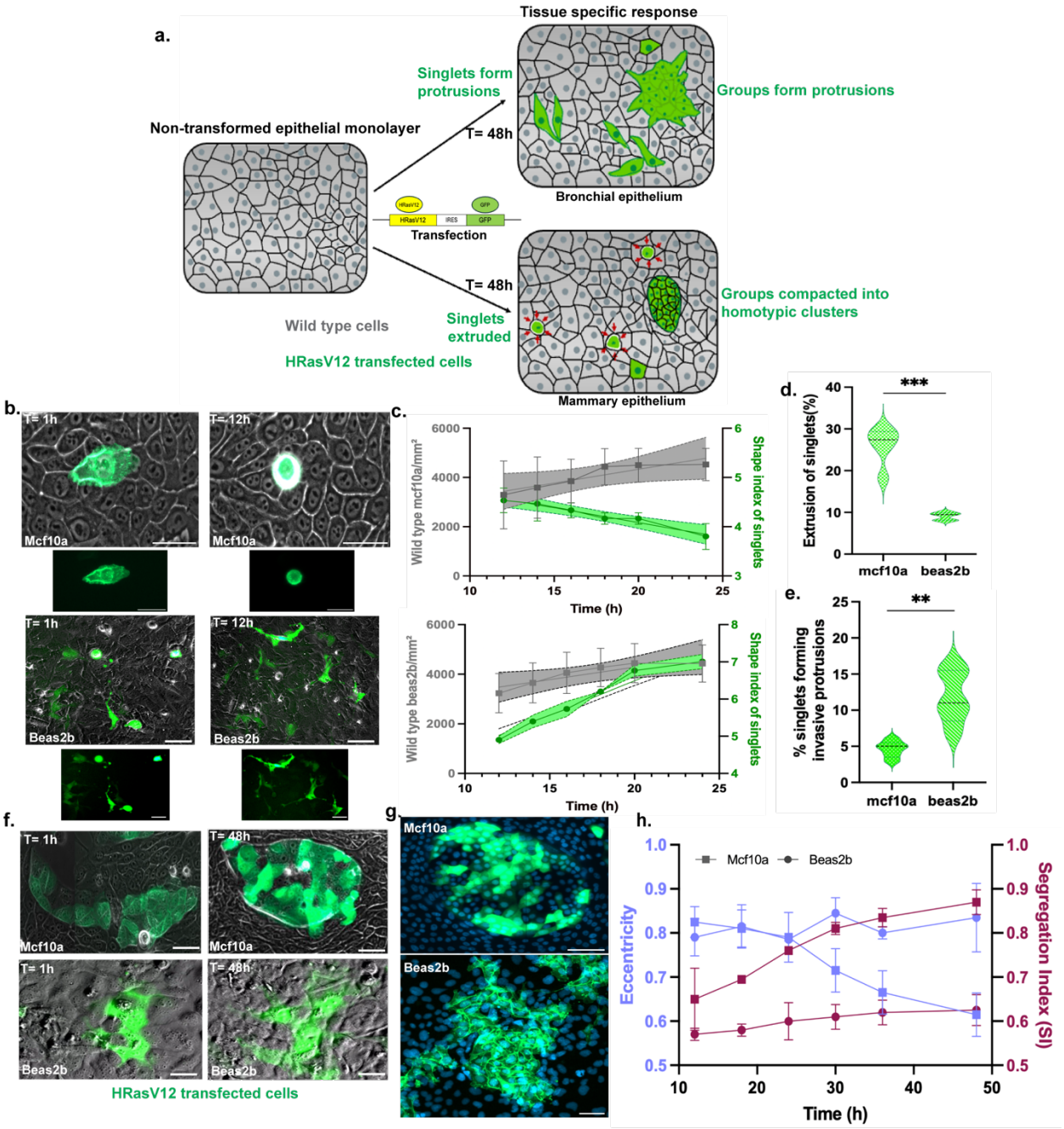

Figure 1: ***Tissue-specific outcomes of HRas^{V12} oncogenic mutants in epithelial monolayers*** (a) Schematic representation of the experimental setup and outcome (b) Representative images showing extrusion of single oncogenic cells (singlets) in mammary epithelium (*upper panel*), but protrusive behavior of the same oncogenic singlets in bronchial epithelium (*bottom panel*) (c) Quantification of shape indices of HRas^{V12} singlets showing reduction in shape indices, with increasing wild-type cell density in mammary epithelium (*upper panel*), but the opposite trend in bronchial epithelium (*bottom panel*), where HRas^{V12} cells continues to spread (d) Extrusion rates of HRas^{V12} singlets are significantly higher in mammary epithelium, while (e) Percentage of HRas^{V12} cells forming protrusions is markedly higher in bronchial epithelium (f) Spreading

of HRas^{V12} in clusters in the two tissues- In mammary epithelium (*upper panel*), clusters become spatially confined, attaining a jammed configuration, while in bronchial epithelium (*bottom panel*), HRasV12 clusters expand, forming long protrusions over time (g) Immunofluorescence images of HRas^{V12} clusters in mammary and bronchial epithelia, highlighting differences in spreading patterns in the two epithelia (h) Quantification of cluster segregation: mammary epithelium exhibits a higher segregation index and reduced eccentricity compared to bronchial epithelium, indicating greater spatial confinement of oncogenic clusters. The segregation index (SI), defined as the average ratio of homotypic and all cell neighbors, quantifies the degree of demixing and is averaged over all cells inside an oncogenic cluster. *Scale bars= 50 µm*

Figure 2: ***Distinct mechanical signatures of HRas^{V12} clusters in mammary and bronchial epithelia***

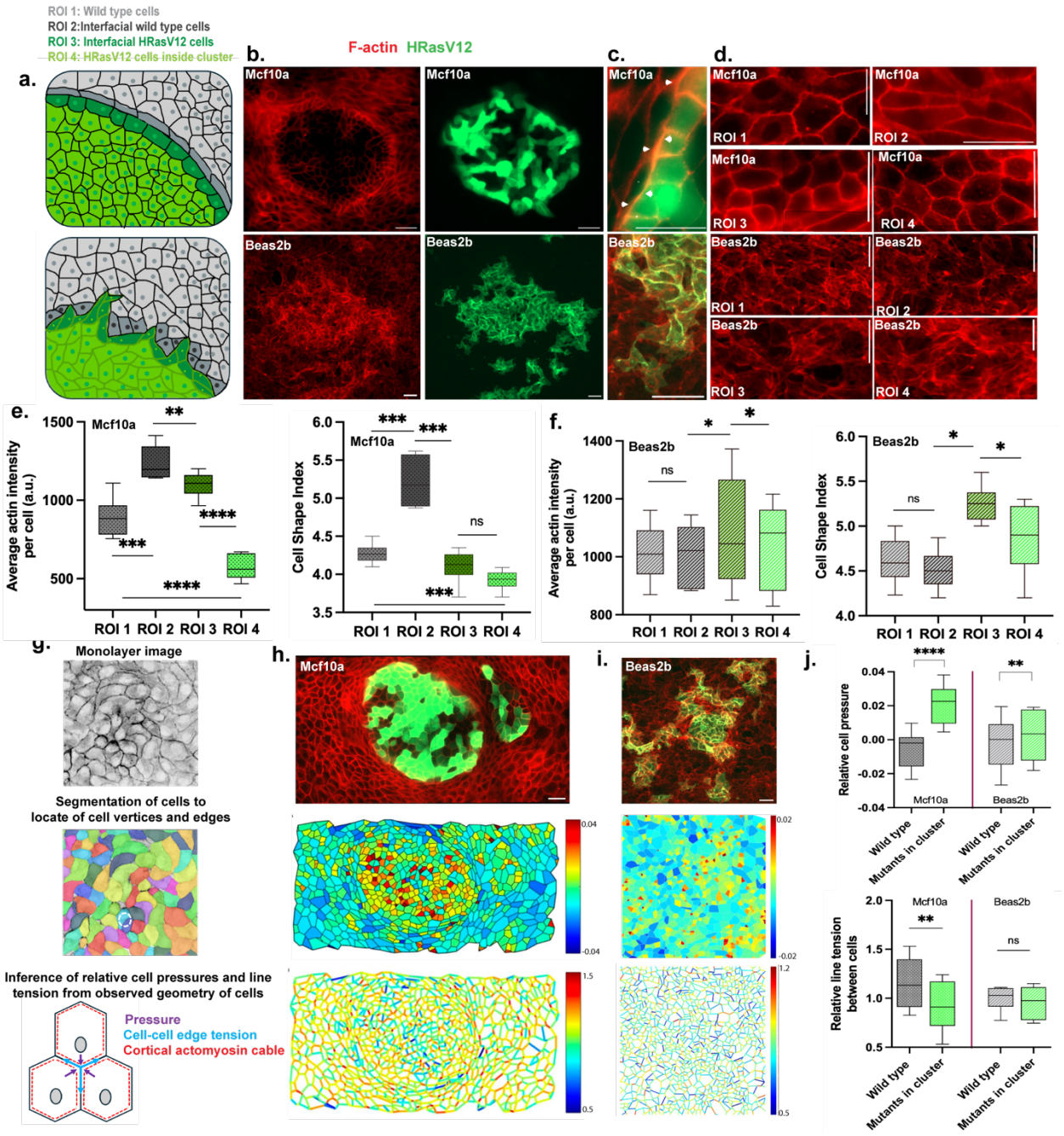

Figure 2: ***Distinct mechanical signatures of HRas^{V12} clusters in mammary and bronchial epithelia***
(a) Representative images showing regions of interest (ROIs) selected for analysis in mammary (*upper panel*) and bronchial epithelia (*lower panel*) (b) Immunofluorescence images of HRas^{V12} clusters stained for F-actin in mammary (*upper panel*) and bronchial epithelia (*lower panel*) (c) Oncogenic cluster–wild-type interface showing distinct actin belt in mammary (*upper panel)* and absence of it in bronchial epithelia (*lower panel)* (d) ROI-based F-actin stained regions of wild-type and oncogenic cells in mammary (upper panel) and bronchial epithelia (lower panel) revealing distinct shape differences in different regions- in mammary epithelia, wild type cells at the interface show elongated shapes (ROI2), and oncogenic cells inside the cluster show jammed shapes (ROI4), in comparison to wild type cells at a random location (ROI1), while in bronchial epithelia, oncogenic cells (ROI 3 and 4) show more elongated shapes compared to wild-type beas2b cells (e), (f) Quantifications of F-actin intensities and shape indices, in mammary epithelia (e), and bronchial epithelia (f), across the four ROIs confirming jammed oncogenic clusters, with unjamming at the interface, in mammary epithelia and unjammed clusters in bronchial epithelia (g) Schematic illustrating the Bayesian Force Inference pipeline used to estimate relative intracellular pressure and cell–cell edge tension (h) Heatmaps depicting relative cell pressures and cell–cell edge tensions in mammary epithelium, revealing localized mechanical heterogeneity (i) Heatmaps of relative cell pressures and edge tensions in bronchial epithelium, showing a distinct mechanical landscape compared to mammary epithelium (j) Quantification of relative intracellular pressures and cell–cell edge tensions across the four ROIs in mammary (upper panel) and bronchial epithelia (lower panel) highlighting tissue-specific differences. *Scale bars= 50 μm*

Figure 3: ***Particle Image Velocimetry (PIV) reveals distinct cellular movement patterns in HRas^{V12} clusters in the two monolayers***

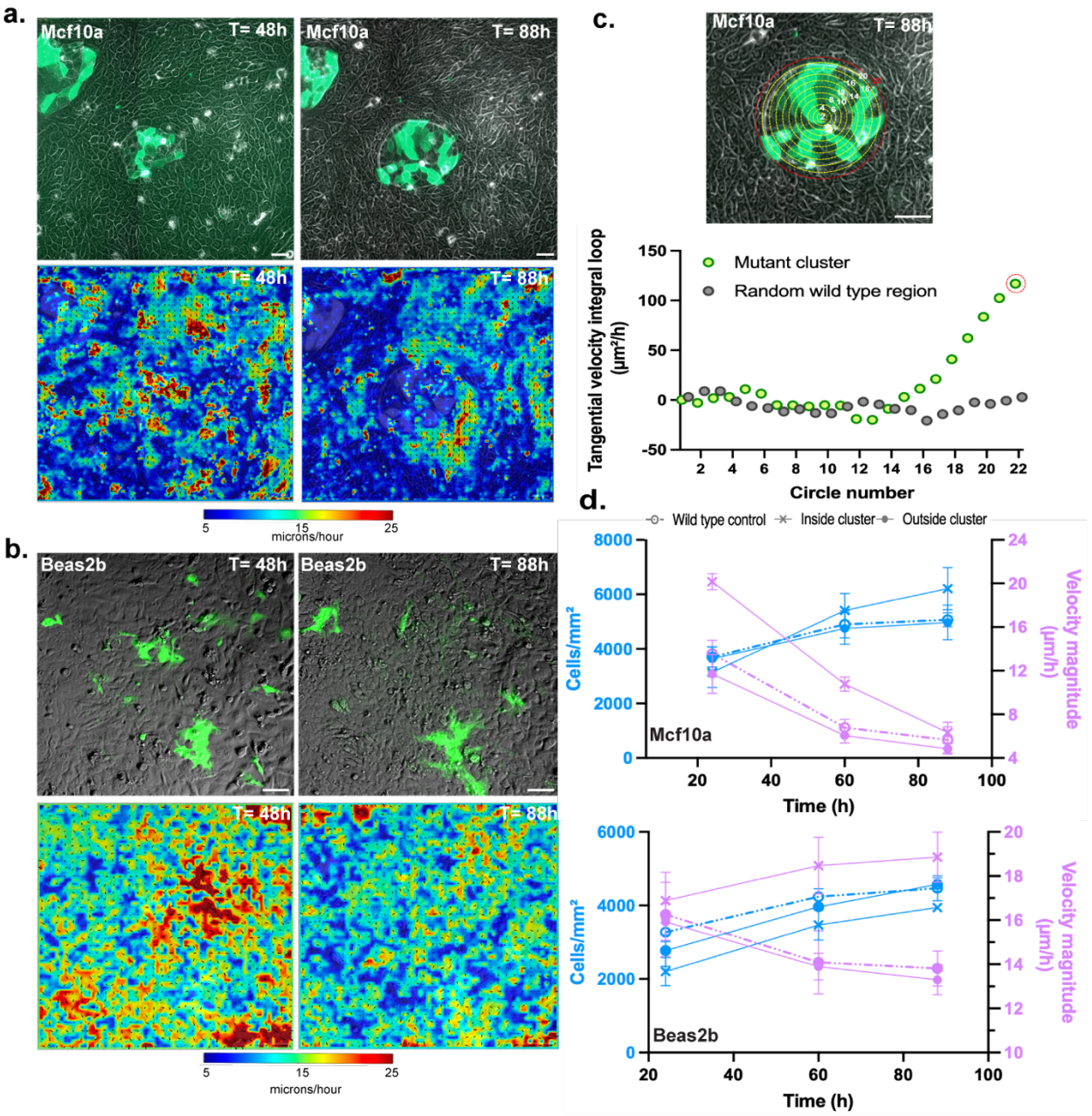

Figure 3: ***Particle Image Velocimetry (PIV) reveals distinct cellular movement patterns in HRas^{V12} clusters in the two monolayers*** (a), (b) Representative snapshots of HRas^{V12} clusters, and the corresponding PIV maps, in mammary (a) and bronchial epithelium (b), as the density of wild type cells increase showing higher velocity attributed to tangential motion in wild type cells along the interface in mammary epithelium, but kinetically arrested state in bronchial epithelium (c) Oncogenic cluster in mcf10a monolayer with concentric circles drawn from the centre of the cluster, radially outward till its boundary (upper panel) and

plot showing tangential motion (expressed as a function of the circles), revealing highest tangential motion along the interface of oncogenic cluster with the wild-type cells in mammary epithelia (lower panel). No significant tangential motion in random wild-type region (c) Representative snapshots of $HRas^{V12}$ clusters in bronchial epithelium at the same two time points and the corresponding PIV velocity maps (d) Quantification of cellular velocities in local regions as cell densities reach confluency showing oncogenic cells clustered in mammary epithelium (*top panel*) jam and show a significant reduction in velocities. In bronchial epithelium (*bottom panel*) while wild type cells show reduced movement as cell density increased- transformed cells continued to show higher motion, signifying jamming of wild type cells have no effect on mutants. *Scale bars= 50 μm*

Figure 4: ***Bi-disperse vertex model reveals interfacial tension-driven segregation of oncogenic clusters***

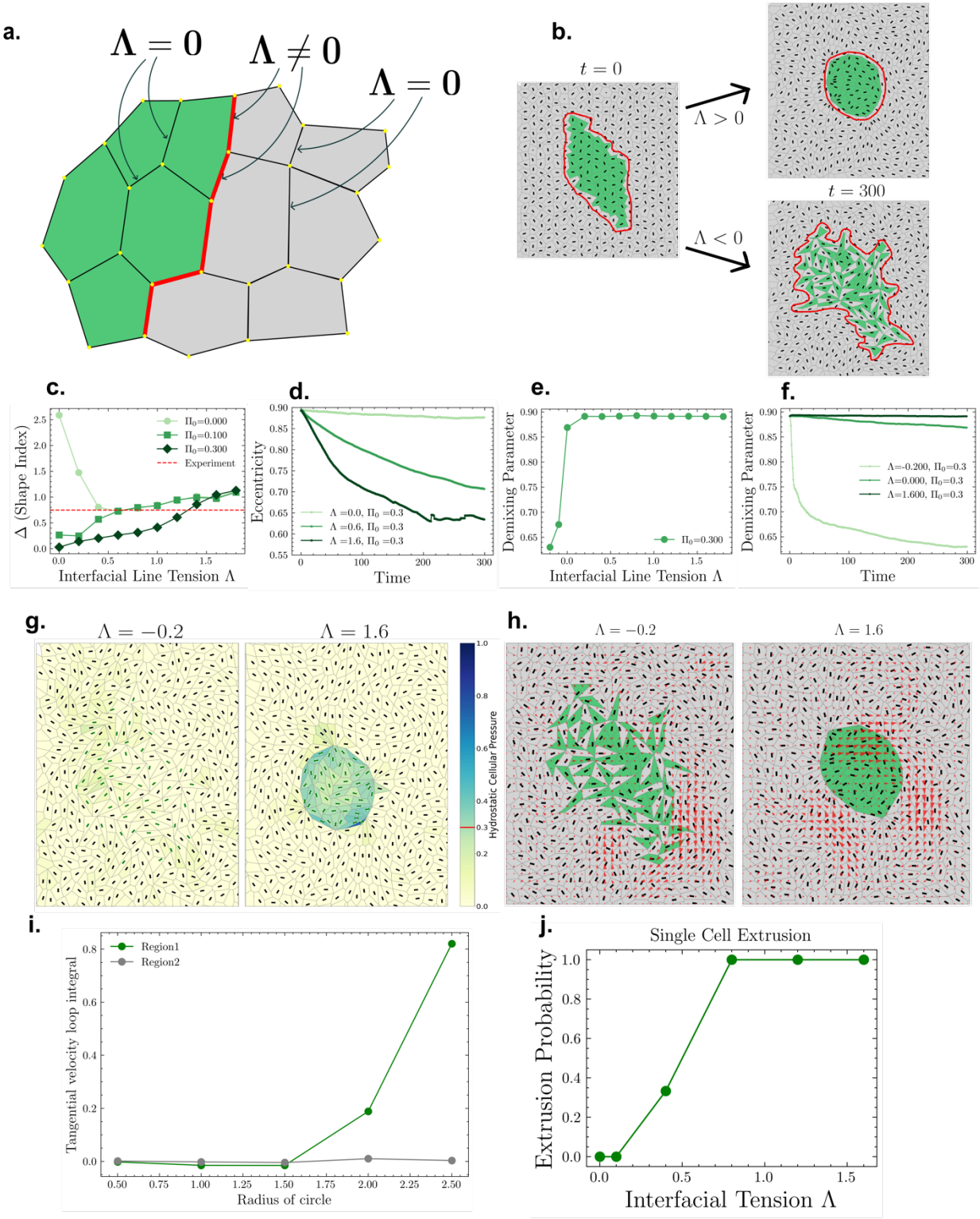

Figure 4: ***Bi-disperse vertex model reveals interfacial tension-driven segregation of oncogenic clusters***

(a) Schematic of the bi-disperse vertex model, where interfacial line tension (red) is applied at the boundary

between mutant (green) and wild-type (grey) (b) The value of Λ determines whether the mutant cluster remains compact or spreads into the wild-type population, where the red line gives the outline of the morphology of the mutant cluster interface (c) Difference in shape index between interfacial and bulk cells as a function of Λ (interfacial tension), shown for different stress thresholds. Experimental average (red) overlaid for comparison (d) Eccentricity of mutant clusters (given by the red lines in (b)) over time for different values of Λ (with $\Pi_0 = 0.3$), indicating changes in cluster morphology (e) Demixing parameter at t = 300 as a function of Λ for$\Pi_0 = 0.3$, quantifying the extent of cluster segregation (f) Time evolution of the demixing parameter for different values of Λ (with $\Pi_0 = 0.3$), demonstrating interfacial tension-driven segregation (g) Hydrostatic pressure maps of mutant and wild-type cells at t = 300, with mutant cells labeled by green directors and wild-type cells by black directors (h) Velocity field maps of epithelial monolayers for different values of Λ, revealing flow patterns around oncogenic clusters (i) Tangential velocity loop integral for circles of varying radius centered at the mutant cluster (Region 1) and centered away from the cluster (Region 2), showing tissue-specific velocity variations (j) Extrusion probability of a single mutant cell as a function of Λ, demonstrating how interfacial tension influences mutant cell fate.

Figure 5: ***Actomyosin belt disruption prevents mutant cluster compaction in mammary epithelia***

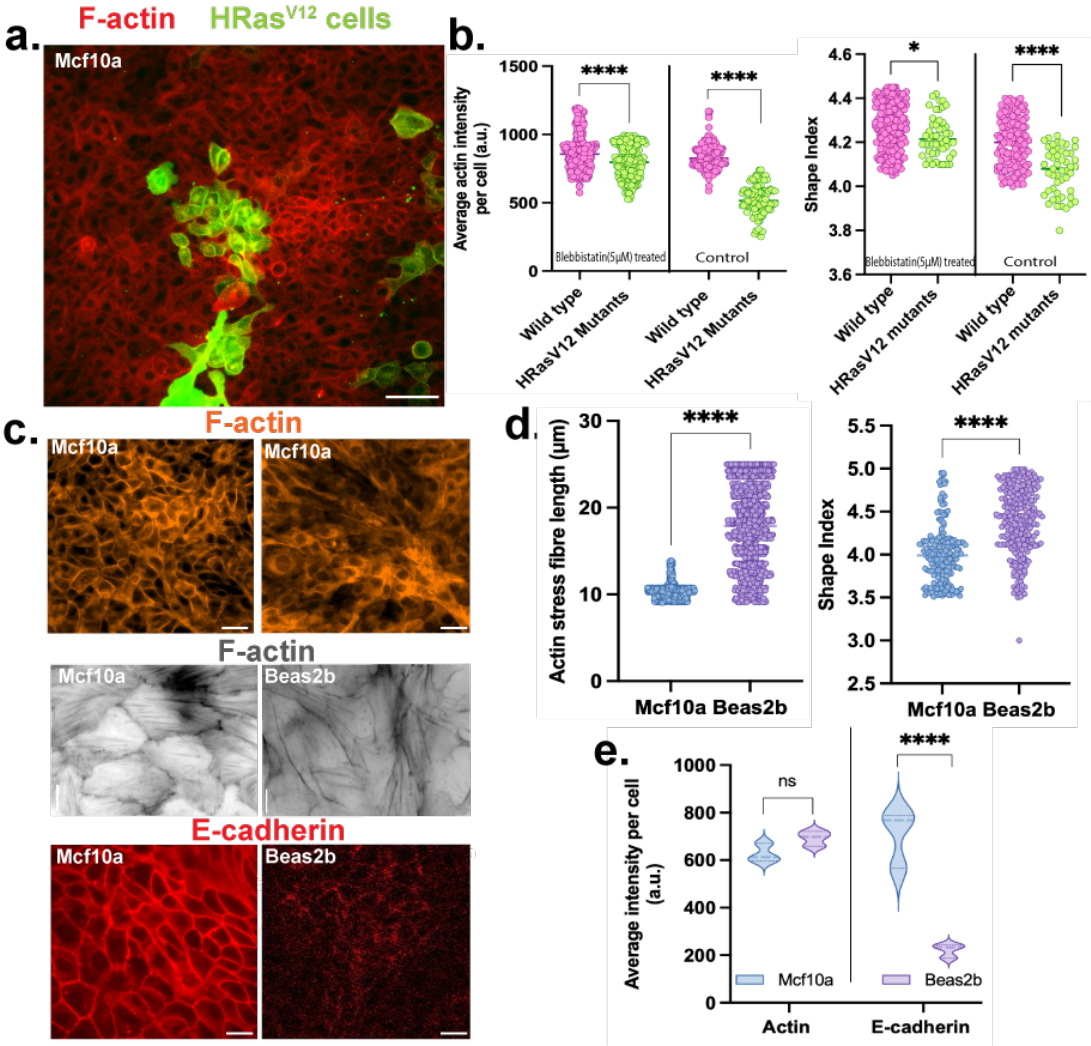

Figure 5: ***Actomyosin belt disruption prevents mutant cluster compaction in mammary epithelia*** (a) Representative actin staining image upon blebbistatin treatment, done after oncogenic induction in mammary epithelial monolayer, showing an absence of an actin belt (b) Quantification of F-actin intensities (left) and shape indices (right), showing difference between oncogenic clusters and wild-type cells in these parameters, is getting small – although not completely vanished because of low concentration of blebbistatin used for the experiment (c) Representative actin and E-cadherin staining images of the wild type monolayers showing longer stress fibers, and an unjammed monolayer in beas2b epithelia, but jamming in Mcf10a. E-cadherin staining aligned with this, and reduced E-cadherin staining in beas2b represent reduced cortical tension in the monolayer. *Scale bars= 50 μm*.

Supplementary

Supplementary Figure 1: ***Myosin belt and per cell myosin intensities***

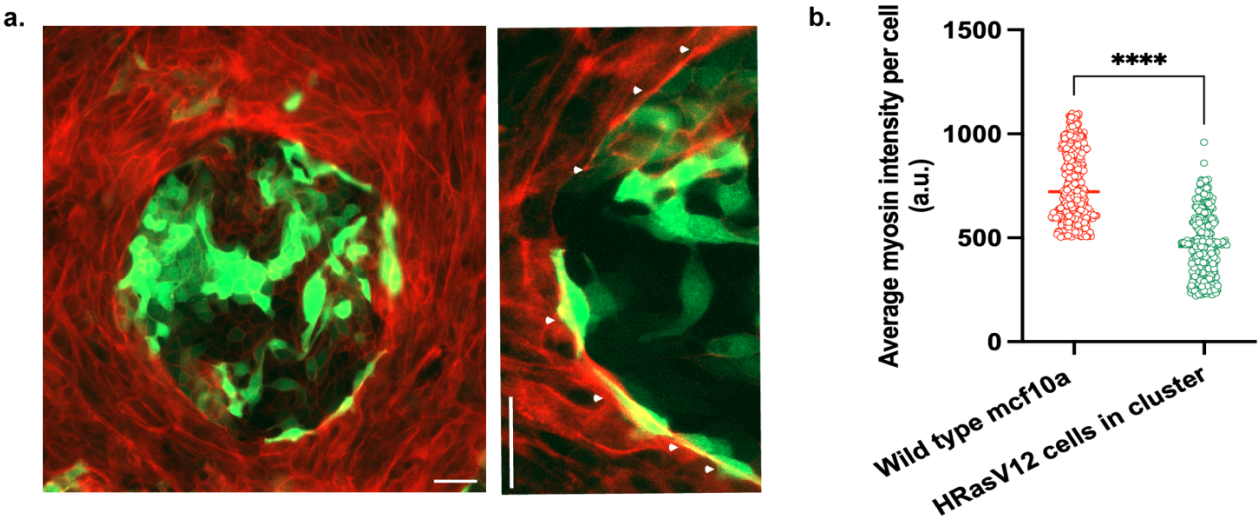

Supplementary Figure 1: ***Myosin belt and per cell myosin intensities*** (a) Images of HRasV12 cluster in mammary epithelia stained for phosphomyosin (left panel) and phosphomyosin belt around the cluster (right panel) (b) Plot showing lower phosphpmyosin levels inside oncogenic clusters in mcf10a. *Scale bars= 50 µm.*

Supplementary Figure 2: ***PIV maps of wild-type mammary and bronchial epithelial monolayers with increasing cell density***

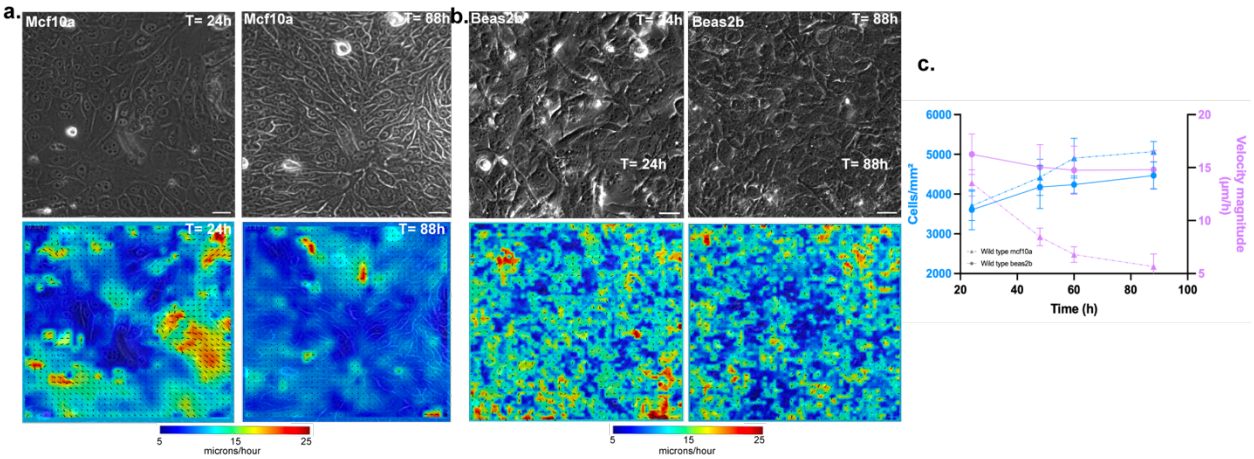

Supplementary Figure 2: ***PIV maps of wild-type mammary and bronchial epithelial monolayers with increasing cell density*** (a) Representative time-lapse images of wild-type (control) mammary epithelium at two different time points, with corresponding PIV velocity maps showing a reduction in overall velocity as cell density increases (b) Representative time-lapse images of wild-type (control) bronchial epithelium at two different time points, with corresponding PIV velocity maps demonstrating a similar reduction in velocity with increasing cell density (c) Quantification of velocity reduction in wild-type mammary and bronchial epithelia as a function of cell density, highlighting tissue-specific differences in collective cell dynamics. *Scale bars= 50 μm.*

Supplementary figure 3:

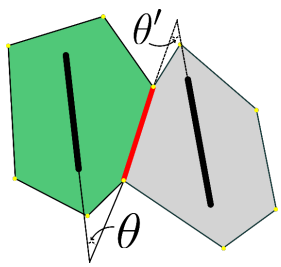

Supplementary figure 3: Illustration of shape-tension coupling at the mutant (green)–wild-type (gray) interface (red), where angles θ_1 and θ_2 represent the orientation of boundary cells relative to their shared edge